The Astrophysical Journal, 937:25 (15pp), 2022 September 20 https://doi.org/10.3847/1538-4357/ac83b2

Influence of Thomson Electron Scattering Redistribution on Spectral Line Polarization Formed in Spherically Symmetric Extended and Expanding Atmospheres

M. Sampoorna[1], A. Megha[2], and H. D. Supriya[3,4]
[1] Indian Institute of Astrophysics, Koramangala, Bengaluru 560 034, India; sampoorna@iiap.res.in
[2] Inter-University Centre for Astronomy and Astrophysics, Post Bag-4, Ganeshkhind, Pune 411007, India
[3] Instituto de Astrofísica de Canarias, E-38205, La Laguna, Tenerife, Spain
[4] Departamento de Astrofísica, Universidad de La Laguna, E-38206 La Laguna, Tenerife, Spain
Received 2022 May 4; revised 2022 July 20; accepted 2022 July 21; published 2022 September 20

Abstract

Scattering of line photons by ambient electrons in thermal motion in the stellar atmosphere modifies the wings of both intensity and linear polarization profiles of the spectral lines. The aim of the present paper is to investigate in detail the influence of Thomson electron scattering redistribution on resonance line polarization formed in spherically symmetric extended and expanding atmospheres. A comoving frame method based on the accelerated lambda iteration technique is used to solve the concerned spherically symmetric polarized transfer equation including both the atomic and Thomson electron scattering redistribution functions. Our numerical studies highlight the importance of accounting for Thomson electron scattering redistribution in spectral line polarization problems.

Unified Astronomy Thesaurus concepts: Stellar atmospheres (1584); Radiative transfer (1335); Spectropolarimetry (1973); Computational methods (1965); Radiative transfer simulations (1967)

1. Introduction

Early-type hot stars are known to possess highly extended as well as expanding atmospheres (see Hubeny & Mihalas 2015). In such atmospheres, which are more often represented by a spherically symmetric medium, the Thomson electron scattering is one of the main sources of opacity. In the reference frame of the electron, the Thomson scattering is frequency coherent. However, when the thermal motion of the electron is taken into account, the scattered photons get redistributed in frequency according to the resulting electron scattering redistribution function.[5] This redistribution of line photons caused by Thomson electron scattering is known to significantly affect the spectral line wings (see, e.g., Hummer & Mihalas 1967; Mihalas et al. 1976).

In previous studies, the influence of Thomson electron scattering redistribution has been extensively investigated in the case of unpolarized transfer in expanding spherical atmospheres (see, e.g., Mihalas et al. 1976; Hillier 1991). As for the polarized line transfer, such investigations have been made mainly for the case of planar static atmospheres (see, e.g., Nagendra et al. 1993; Supriya et al. 2012, and citations therein). On the other hand, the influence of Thomson electron scattering redistribution on polarized line profiles formed in spherically symmetric static or expanding atmospheres remains sparsely explored. An exception to this is the work by Hillier (1996), who considers polarized line and continuum transfer in stars with extended and expanding envelopes accounting for the effects of Thomson electron scattering redistribution, but assuming an intrinsically unpolarizable line. In other words polarization in both the line and continuum was assumed to arise purely from Thomson electron scattering. In the present paper we however consider an intrinsically polarizable line and the problem of polarized spectral line transfer in extended and expanding spherically symmetric atmospheres including the influence of Thomson electron scattering redistribution.

The aforementioned problem for the case of pure resonance line scattering was considered in Megha et al. (2019), wherein a comoving frame (CMF) method was developed to solve the concerned polarized line transfer equation in spherically symmetric expanding atmospheres. Here, in addition to the atomic scattering we include the scattering of line photons by ambient thermal electrons and discuss their influence on line polarization formed in spherically symmetric static as well as moving media.

The structure of the present paper is as follows. In Section 2, we present the basic equations of the problem at hand and briefly outline the numerical method of solution. The influence of Thomson electron scattering redistribution on line polarization is studied in detail in Section 3, and the conclusions are presented in Section 4.

2. Polarized Transfer Equation and Solution Method

A polarized radiation field in a one-dimensional spherically symmetric atmosphere with or without nonrelativistic radial velocity fields is described by the Stokes vector $\boldsymbol{I} = (I, Q)^{\mathrm{T}}$, with I denoting the intensity and Q the linear polarization. In such an atmosphere the polarized radiation field is azimuthally symmetric. Furthermore, we define the reference direction for negative Q as parallel to the nearest limb.

For an observer comoving with the medium at radius r, the radiative transfer equation for the polarized radiation of frequency ν, and flowing in a direction μ defined by the cosine of the angle θ with the radius vector is given by (see,

[5] The explicit form of the electron scattering redistribution function is given by the unnumbered equations in pp. 420 and 432 of Mihalas (1978) for the angle-dependent and the angle-averaged cases, respectively. In the present paper we consider only the angle-averaged case.

e.g., Equation (19.176) in p. 725 of Hubeny & Mihalas 2015)

$$\mu\frac{\partial \boldsymbol{I}(r,\,\mu,\,\nu)}{\partial r}+\frac{(1-\mu^2)}{r}\frac{\partial \boldsymbol{I}(r,\,\mu,\,\nu)}{\partial \mu}-\frac{\nu_0 v_r}{cr}\left[(1-\mu^2)+\mu^2\frac{r}{v_r}\frac{dv_r}{dr}\right]\frac{\partial \boldsymbol{I}(r,\,\mu,\,\nu)}{\partial \nu}=-\chi(r,\,\nu)[\boldsymbol{I}(r,\,\mu,\,\nu)-\boldsymbol{S}(r,\,\mu,\,\nu)], \quad (1)$$

where ν_0 is the line-center frequency, v_r is the nonrelativistic radial velocity field, and c is the speed of light. The third term on the left-hand-side of the above equation containing the frequency derivative of the Stokes vector represents the CMF term, which accounts only for the Doppler shift effects in the nonrelativistic regime. In the presence of absorption in a spectral line arising from a transition in a two-level atom (with line-integrated absorption coefficient $\chi_l(r)$), in the background continuum (with coefficient $\chi_c(r)$), and the electron scattering opacity (with coefficient $\chi_e(r)$), the total absorption coefficient is given by $\chi(r,\ \nu)=\chi_l(r)\varphi(\nu)+\chi_c(r)+\chi_e(r)$. All three coefficients (namely, χ_l, χ_c, and χ_e) are assumed to vary as r^{-2}, which is a reasonable choice in a spherical atmosphere. The line absorption profile $\varphi(\nu)$ is the standard normalized Voigt profile function.

In a stellar atmosphere intrinsically polarizable lines are polarized due to resonance scattering on atoms and molecules (Stenflo 1994), while the continuum is polarized due to Rayleigh scattering on neutral hydrogen, helium, and molecules, and Thomson scattering on electrons (see, e.g., Fluri & Stenflo 1999; Stenflo 2005; Kostogryz & Berdyugina 2015; Kostogryz et al. 2016). In the present paper polarization due to resonance scattering on atomic lines and Thomson scattering on electrons are treated in detail through the use of corresponding redistribution functions. The continuum contributions other than Thomson scattering on electrons are treated as unpolarized. This is partly justified by the fact that in a hot stellar atmosphere (like in early-type stars) electron scattering opacity dominates. Nevertheless the scattering opacity due to Rayleigh scattering on neutral hydrogen and helium also contributes (see, e.g., Figures 2(e) and 2(f) of Kostogryz et al. 2016). Since the aim of the present paper is to isolate the influence of Thomson electron scattering redistribution on resonance line polarization, here we assume an unpolarized background continuum. In a future extension of the present work, we plan to include the contribution from the polarized background continuum arising from Rayleigh scattering on neutral hydrogen and helium.

The total source vector for scattering of line photons on a two-level atom and ambient electrons along with an unpolarized background continuum is given by

$$\boldsymbol{S}(r,\,\mu,\,\nu)=\frac{\varphi(\nu)\boldsymbol{S}_l(r,\,\mu,\,\nu)+\beta_c\boldsymbol{S}_c+\beta_e\boldsymbol{S}_e(r,\,\mu,\,\nu)}{\varphi(\nu)+\beta_c+\beta_e}, \quad (2)$$

where $\beta_c=\chi_c/\chi_l$ and $\beta_e=\chi_e/\chi_l$. The line source vector can be written as

$$\boldsymbol{S}_l(r,\,\mu,\,\nu)=\epsilon B_{\nu_0}\boldsymbol{U}+\int_0^\infty d\nu'\frac{1}{2}\int_{-1}^{+1}d\mu'\frac{\boldsymbol{R}_{\rm a}(\nu,\,\mu,\,\nu',\,\mu')}{\varphi(\nu)}\boldsymbol{I}(r,\,\mu',\,\nu'). \quad (3)$$

Here ϵ is the thermalization parameter, B_{ν_0} is the Planck function at the line center, and $\boldsymbol{U}=(1,\ 0)^{\rm T}$. The atomic redistribution matrix $\boldsymbol{R}_{\rm a}$ for resonance scattering on a two-level atom with an infinitely sharp lower level is given in Bommier (1997; see also Domke & Hubeny 1988). The unpolarized continuum source vector $\boldsymbol{S}_c=B_{\nu_0}\boldsymbol{U}$. The electron scattering source vector has the form

$$\boldsymbol{S}_e(r,\,\mu,\,\nu)=\int_0^\infty d\nu'\frac{1}{2}\int_{-1}^{+1}d\mu'\boldsymbol{R}_{\rm e}(\nu,\,\mu,\,\nu',\,\mu')\boldsymbol{I}(r,\,\mu',\,\nu'). \quad (4)$$

The electron scattering redistribution matrix is given by

$$\boldsymbol{R}_{\rm e}(\nu,\,\mu,\,\nu',\,\mu')=\mathbf{P}_{\rm R}(\mu,\,\mu')R_{\rm e,AA}(\nu,\,\nu'), \quad (5)$$

where $\mathbf{P}_{\rm R}$ is the Rayleigh phase matrix (see Chandrasekhar 1950) and $R_{\rm e,AA}(\nu,\,\nu')$ is the angle-averaged electron scattering redistribution function (see unnumbered equations in p. 432 of Mihalas 1978; see also Hummer & Mihalas 1967; Auer & Mihalas 1968), given by

$$R_{\rm e,AA}(\nu,\,\nu')=\frac{1}{w_{\rm e}}\,{\rm ierfc}\left|\frac{\nu-\nu'}{2w_{\rm e}}\right|, \quad (6)$$

where $w_{\rm e}$ is the electron Doppler width and ierfc is the iterated complementary error function of the form

$${\rm ierfc}(t)=\frac{1}{\sqrt{\pi}}\,{\rm e}^{-t^2}-t\,{\rm erfc}(t). \quad (7)$$

Following Hummer & Rybicki (1971), we solve the polarized transfer Equation (1) by the tangent-ray method, namely in the so-called (p,z) coordinate system, wherein p is the impact parameter and z is the distance along the tangent ray (see Figure 1 of Megha et al. 2019). Furthermore, for computational simplicity we consider the irreducible spherical tensor representation of the Stokes and the source vectors (Frisch 2007). We define the monochromatic optical depth along the tangent ray as $d\tau(z,\,\nu)=-\chi(r,\,\nu)dr/\mu=-\chi(r,\,\nu)\,dz$. Equation (1) can now be rewritten in the $(p,\,z)$ coordinate system as

$$\pm\frac{\partial \boldsymbol{\mathcal{I}}^{\pm}(z,\,p,\,\nu)}{\partial\tau(z,\,\nu)}=\boldsymbol{\mathcal{I}}^{\pm}(z,\,p,\,\nu)-\boldsymbol{\mathcal{S}}(z,\,\nu)-\tilde{\boldsymbol{\mathcal{S}}}(z,\,p,\,\nu). \quad (8)$$

The irreducible Stokes vector for the outgoing "+" and incoming "−" tangent rays is denoted by $\boldsymbol{\mathcal{I}}^{\pm}$ with components $\mathcal{I}_0^{0,\pm}$ and $\mathcal{I}_0^{2,\pm}$. In the irreducible spherical tensor representation, the total source vector $\boldsymbol{S}(r,\,\mu,\,\nu)$ takes the form

$$\boldsymbol{\mathcal{S}}(z,\,\nu)=\frac{\varphi(\nu)\boldsymbol{\mathcal{S}}_L(z,\,\nu)+\beta_c\boldsymbol{\mathcal{S}}_c}{\varphi(\nu)+\beta_c+\beta_e}, \quad (9)$$

where $\boldsymbol{\mathcal{S}}_c=B_{\nu_0}\boldsymbol{U}$ and

$$\boldsymbol{\mathcal{S}}_L(z,\,\nu)=\epsilon B_{\nu_0}\boldsymbol{U}+\int_0^\infty d\nu'\frac{1}{2}\int_{-1}^{+1}d\mu'\frac{\tilde{\boldsymbol{\mathcal{R}}}(\nu,\,\nu')}{\varphi(\nu)}\boldsymbol{\Psi}(\mu')\boldsymbol{\mathcal{I}}(z,\,\mu',\,\nu'). \quad (10)$$

In the above equation we have combined the line and electron scattering source vectors into a single source vector to facilitate the application of the operator perturbation method (see Supriya et al. 2012, for more details). The Rayleigh phase matrix in the irreducible basis is denoted by $\boldsymbol{\Psi}(\mu)$ (Frisch 2007). The (2×2) combined redistribution matrix in the irreducible

basis is given by

$$\tilde{\boldsymbol{\mathcal{R}}} = \mathrm{diag}[\mathcal{R}^0_{0,a} + \beta_e R_{\mathrm{e,AA}}, \mathcal{R}^2_{0,a} + \beta_e R_{\mathrm{e,AA}}], \tag{11}$$

where

$$\mathcal{R}^K_{0,a} = W_K\{\alpha R_{\mathrm{II,AA}} + [\beta^{(K)} - \alpha] R_{\mathrm{III,AA}}\}, \tag{12}$$

with $K = 0,2$. Here $R_{\mathrm{II,AA}}$ and $R_{\mathrm{III,AA}}$ are the angle-averaged partial frequency redistribution (PRD) functions of Hummer (1962). Their explicit forms are given respectively by Equations (13.64) in p. 428 and (13.67) in p. 430 of Mihalas (1978). The branching ratios α and $\beta^{(K)}$ are given by (Bommier 1997)

$$\alpha = \frac{\Gamma_{\mathrm{R}}}{\Gamma_{\mathrm{R}} + \Gamma_{\mathrm{I}} + \Gamma_{\mathrm{E}}}, \tag{13}$$

$$\beta^{(K)} = \frac{\Gamma_{\mathrm{R}}}{\Gamma_{\mathrm{R}} + \Gamma_{\mathrm{I}} + D^{(K)}}, \tag{14}$$

where Γ_{R} and Γ_{I} denote, respectively, the radiative and inelastic collisional deexcitation rates; Γ_{E} and $D^{(K)}$ are the elastic and depolarizing collisional rates, respectively; W_K is the atomic polarizability factor (with $W_0 = 1$). For a normal Zeeman triplet considered in this paper $W_2 = 1$.

In Equation (8), the CMF term is denoted by $\tilde{\boldsymbol{\mathcal{S}}}(z, p, \nu)$ and is given by

$$\tilde{\boldsymbol{\mathcal{S}}}(z, p, \nu) = \gamma(r, p, \nu)\, \frac{\partial \boldsymbol{\mathcal{I}}^{\pm}(z, p, \nu)}{\partial \nu}, \tag{15}$$

where

$$\gamma(r, p, \nu) = \frac{\nu_0 v_{\mathrm{th}}}{c\, \chi(r, \nu)} \left[(1 - \mu^2)\frac{V}{r} + \mu^2 \frac{dV}{dr}\right]. \tag{16}$$

Here v_{th} is the thermal velocity assumed to be constant throughout the spherical atmosphere and $V = v_r/v_{\mathrm{th}}$. As in Mihalas et al. (1975), here we first define a frequency grid with NF number of points. The frequency points are labeled as ν_m with $m = 1, 2, \ldots,$ NF in order of decreasing values, namely $\nu_1 > \nu_2 > \ldots > \nu_{\mathrm{NF}}$. The nondimensional frequency grid $x_m = (\nu_m - \nu_0)/\Delta\nu_{\mathrm{D}}$ (with ν_0 being the line-center frequency and $\Delta\nu_{\mathrm{D}}$ the atomic Doppler width) is then constructed from the ν_m grid. At any point O on the z grid corresponding to a given impact parameter ray p, we discretize the frequency derivative using a local upwind scheme:

$$\left[\frac{\partial \boldsymbol{\mathcal{I}}^{\pm}}{\partial \nu}\right]_{\mathrm{O},\nu_m} = \frac{\boldsymbol{\mathcal{I}}^{\pm}_{\mathrm{O}}(p, \nu_m) - \boldsymbol{\mathcal{I}}^{\pm}_{\mathrm{O}}(p, \nu_{m\mp1})}{\nu_m - \nu_{m\mp1}}, \tag{17}$$

where ν_{m-1} is used when $\gamma \geqslant 0$ and ν_{m+1} is used when $\gamma < 0$. Using the parabolic and linear interpolations for $\boldsymbol{\mathcal{S}}$ and $\tilde{\boldsymbol{\mathcal{S}}}$, respectively (Hauschildt & Baron 2004), the short-characteristic formal solution in the CMF is given by

$$\begin{aligned}
&\left\{1 - \Psi'^{,\pm}_{\mathrm{O}}[\gamma(r, p, \nu_m)]_{\mathrm{O}} \frac{1}{(\nu_m - \nu_{m\mp1})}\right\} \boldsymbol{\mathcal{I}}^{\pm}_{\mathrm{O}}(p, \nu_m) \\
&= e^{-\Delta\tau_{\mathrm{MO}}} \boldsymbol{\mathcal{I}}^{\pm}_{\mathrm{M}}(p, \nu_m) + \delta\boldsymbol{\mathcal{I}}^{\pm}_{\mathrm{O}}(p, \nu_m) + \Psi'^{,\pm}_{\mathrm{M}} \tilde{\boldsymbol{\mathcal{S}}}_{\mathrm{M}}(p, \nu_m) \\
&\quad - \Psi'^{,\pm}_{\mathrm{O}}[\gamma(r, p, \nu_m)]_{\mathrm{O}} \frac{\boldsymbol{\mathcal{I}}^{\pm}_{\mathrm{O}}(p, \nu_{m\mp1})}{(\nu_m - \nu_{m\mp1})}.
\end{aligned} \tag{18}$$

In the above equation $\Delta\tau_{\mathrm{MO}}$ is the optical distance on the segment MO of the short-characteristic MOP stencil, and $\Psi'^{,\pm}_{\mathrm{O}}$ and $\Psi'^{,\pm}_{\mathrm{M}}$ are the linear interpolation weights. The symbol $\delta\boldsymbol{\mathcal{I}}^{\pm}_{\mathrm{O}}(p, \nu_m)$ represents the parabolic interpolation of $\boldsymbol{\mathcal{S}}$ on the MOP stencil. Following Mihalas et al. (1975) the initial condition of $\frac{\partial \boldsymbol{\mathcal{I}}^{\pm}}{\partial \nu} = 0$ is used at the high frequency edge when $\gamma \geqslant 0$ and at the low frequency edge when $\gamma < 0$.

We solve the polarized transfer Equation (8) by applying the Jacobi based CMF polarized accelerated lambda iteration method (Megha et al. 2019). In the presence of electron scattering, however, the core-wing method cannot be applied to compute the source vector corrections. Instead, we use the frequency-by-frequency method of Paletou & Auer (1995) (see also Sampoorna et al. 2008).

3. Numerical Results

In this section we explore in detail the influence of Thomson electron scattering redistribution on polarized line profiles formed in a spherically symmetric isothermal atmosphere characterized by a frequency averaged total radial line optical thickness T and outer radius R in units of core radius R_{core}. As already mentioned, we consider inverse square law opacity distribution for line, continuum, and electron scattering opacities. All the different grid discretizations are identical to those discussed in Megha et al. (2019), hence we do not further elaborate them here. Moreover, we use the reflecting boundary condition in our computations. In the following subsections, we first discuss the nature of the angle-averaged electron scattering redistribution function (see Section 3.1) and then illustrate and discuss the numerical solutions obtained in two cases, namely the case of static atmosphere (see Section 3.2) and the case of expanding atmosphere (see Section 3.3).

3.1. Angle-averaged Electron Scattering Redistribution Function

We recall that the Thomson scattering by an electron is frequency coherent in the rest frame of the electron. When thermal motion of the electron is accounted for, we obtain the electron scattering redistribution function—the angle-averaged version of which is given in Equation (6). In terms of the nondimensional frequency x defined using the atomic Doppler width, this function takes the form:

$$R_{\mathrm{e,AA}}(x, x') = \frac{1}{\omega}\, \mathrm{ierfc}\left|\frac{x - x'}{2\omega}\right|, \tag{19}$$

where $\omega = w_{\mathrm{e}}/\Delta\nu_{\mathrm{D}} = 43\sqrt{A}$, with A being the atomic weight of the atom under consideration. In the present paper, we consider a stellar atmosphere predominantly containing hydrogen, hence $\omega = 43$.

Upper panels of Figure 1 illustrate the functional form of $R_{\mathrm{e,AA}}(x, x')$ for different incoming frequencies x'. For a given incoming frequency x', electron scattering redistribution exhibits a frequency coherent peak at $x = x'$ followed by slowly falling wings, which die down after about two to three electron Doppler widths. Clearly the magnitude and shape of $R_{\mathrm{e,AA}}(x, x')$ is identical for different values of x'. This is expected because $R_{\mathrm{e,AA}}(x, x')$ is a function of only the absolute difference between the outgoing and incoming frequencies (see Equation (19)). As noted in Mihalas et al. (1976), such a behavior is consistent with the frequency independence of the

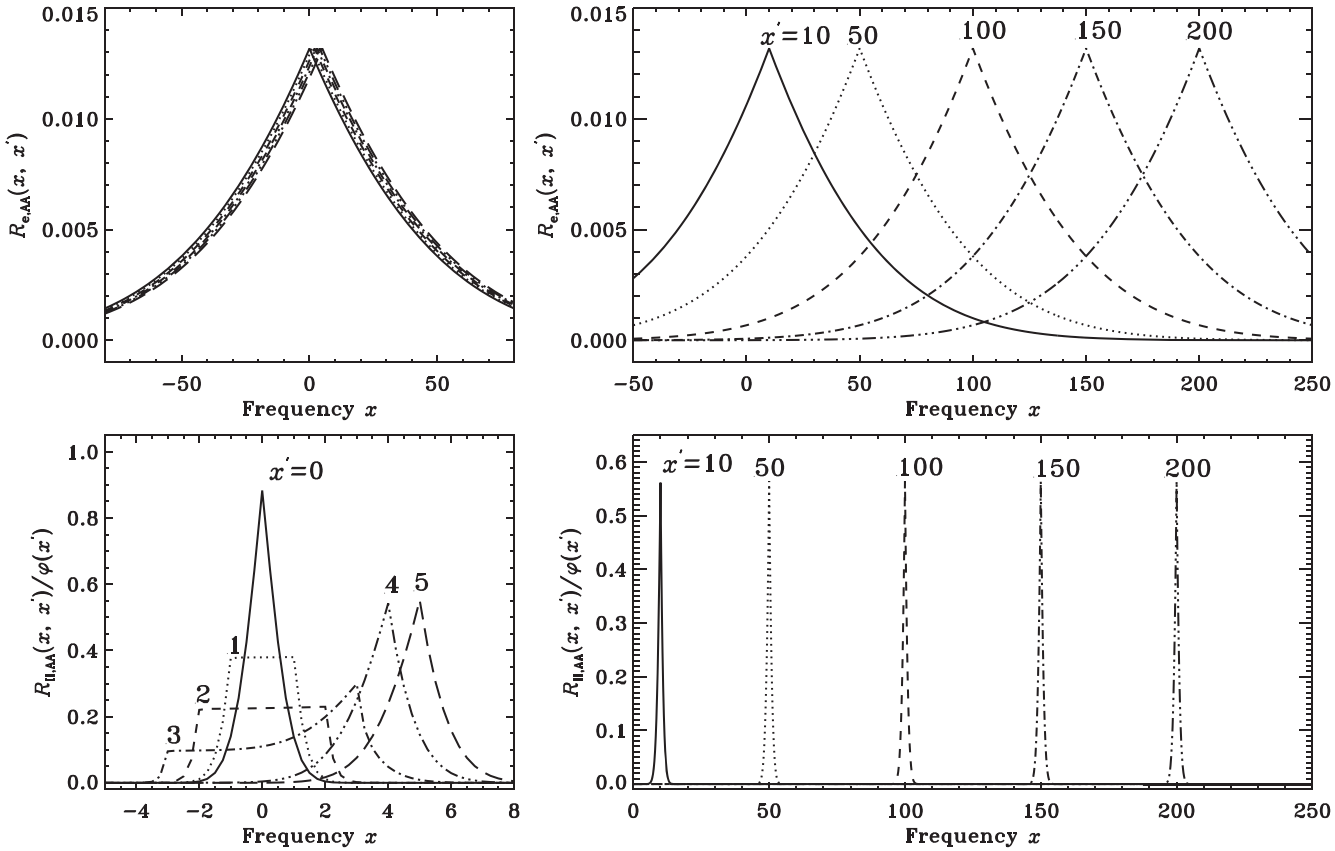

Figure 1. Angle-averaged electron scattering (upper panels) and atomic type-II (lower panels) redistribution functions vs. outgoing frequency x for different incoming frequencies $x' = 0$, 1, 2, 3, 4, 5 (left panels) and $x' = 10$, 50, 100, 150, 200 (right panels). Different line types are indicated in the panels. Different line types in the upper left panel are the same as in the lower left panel.

Thomson cross section. This in turn leads to a never ending redistribution profile. For comparison we present the atomic type-II redistribution function in the lower panels of Figure 1. The absorption profile function is $\varphi(x')$ for resonance scattering on atoms, while it is unity for electron scattering. Therefore, we plot $R_{\rm II,AA}(x, x')/\varphi(x')$ versus x for different x'. Depending on whether the incoming photon is a line core or line wing photon, the atomic type-II redistribution exhibits different behavior. In particular, it exhibits Doppler redistribution and strong noncoherence in the line core and near frequency coherence in the wings (see the lower panels of Figure 1). Thus in the line wings the nature of type-II redistribution is somewhat similar to the electron redistribution. However for a given x' while the electron redistribution dies down after two–three electron Doppler width, the type-II redistribution dies down after two–three atomic Doppler width (which is much smaller than the electron Doppler width). These similarities and differences in the type-II and electron redistribution functions have important implications on the wings of emergent intensity and polarization profiles, that are discussed in the following subsection.

3.2. Static Atmosphere

In the static case the Stokes I and Q are symmetric about the line center. Moreover, the Thomson electron scattering redistribution exhibits its influence predominantly in the near and far wings. Therefore, in this section we illustrate Stokes I and Q/I profiles as a function of the logarithm of nondimensional frequency x, for only positive values of x. The line center is excluded as logarithm of zero is not defined. Furthermore, since the effects of Thomson electron scattering redistribution are more pronounced in the absence of a background continuum, we first consider the pure line case for our studies presented in Figures 2–7 and then illustrate the influence of background continuum in Figures 8–10.

Influence of Thomson electron scattering redistribution on line polarization emerging from a spherically symmetric static medium of different total radial line optical thickness T and outer radius R is shown in Figures 2–4. Like in the planar case (see, e.g., Supriya et al. 2012), frequency coherent peaks in the electron scattering redistribution (see upper panels in Figure 1) give rise to a typical bulge in the wings of the intensity profile (see solid and dotted–dashed lines in Figures 2–4). For a given optical thickness T, this bulge however decreases as the outer radius R increases (compare Figures 2, 3, and 4; see also Tables 1–3). For example, for $T = 10^2$ and $R = 200$, the bulge in the intensity profile has reduced considerably (see Table 3) such that it is invisible graphically (see panel (a) in Figure 4). This is because when R is increased keeping the T and other atmospheric parameters fixed, the medium becomes more and more dilute such that the line photons escape after only a few number of scatterings. In fact, as shown in Kunasz & Hummer (1974) the mean number of scatterings decrease with increasing R.

As for the Stokes Q/I profiles, the influence of Thomson electron scattering redistribution is seen for all the different T and R considered here (compare for example solid and dotted lines in Figures 2–4). Clearly, linear polarization profiles are more sensitive to Thomson electron scattering redistribution

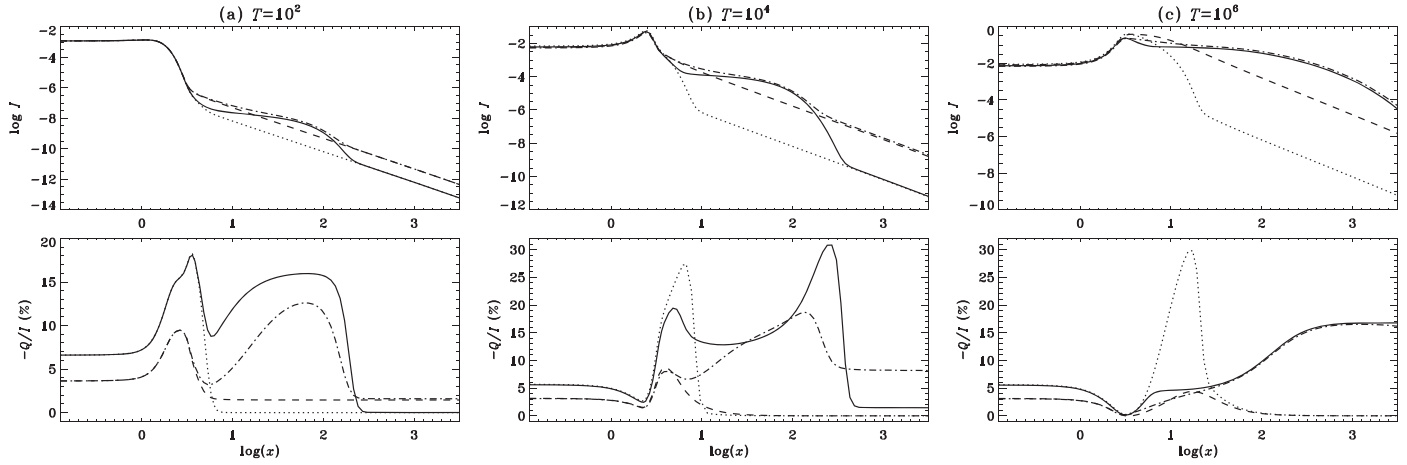

Figure 2. The emergent I and Q/I profiles from a spherically symmetric static medium of outer radius $R = 2$. The line of sight is at $\mu = 0.1$. Panels (a), (b), and (c) correspond, respectively, to $T = 10^2$, 10^4, and 10^6. Other model parameters are $\beta_c = 0$, $\epsilon = 10^{-4}$, and damping parameter $a = 10^{-3}$. Electron scattering opacity $\beta_e = 0$ for dotted and dashed lines, while it is 10^{-5} for solid and dotted–dashed lines. Elastic collision rate Γ_E/Γ_R is zero for solid and dotted lines, while it is unity for dashed and dotted–dashed lines. Depolarizing collision rate $D^{(2)} = 0.5\Gamma_E$.

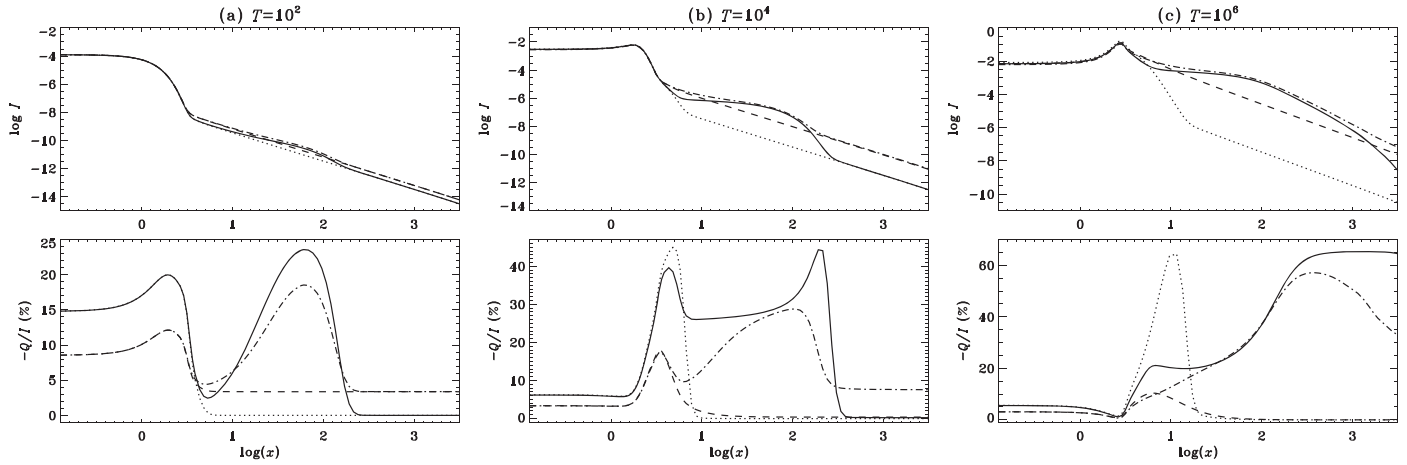

Figure 3. Same as Figure 2, but for $R = 20$.

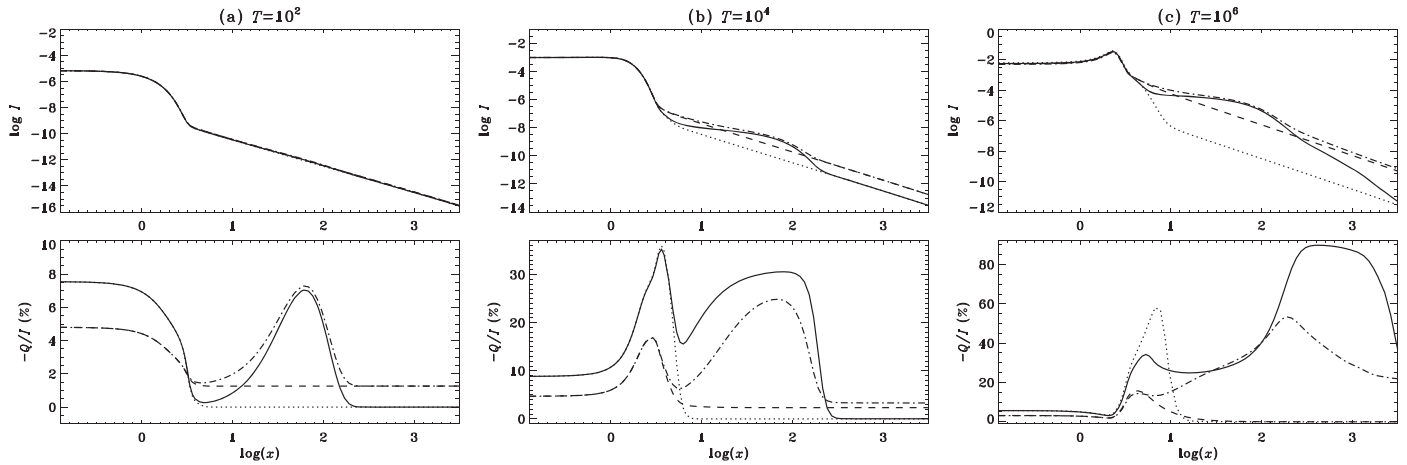

Figure 4. Same as Figure 2, but for $R = 200$.

than the intensity profiles. Like in the planar case (see Supriya et al. 2012), frequency coherent peaks in the electron scattering redistribution (see upper panels in Figure 1) give rise to a secondary peak around $x \gtrsim 60$ in the Q/I profiles (see solid and dotted–dashed lines in Figures 2–4), while the frequency coherent peaks in type-II redistribution (see lower panels in Figure 1) give rise to the near wing PRD peak (at about $|x| \lesssim 20$; occurrence and frequency position of this near wing PRD peak however depends on T and R). The magnitude of this secondary peak as well as the near wing PRD peak in general increases for larger R. This is because as R increases the contribution from the emission lobes of the spherical medium

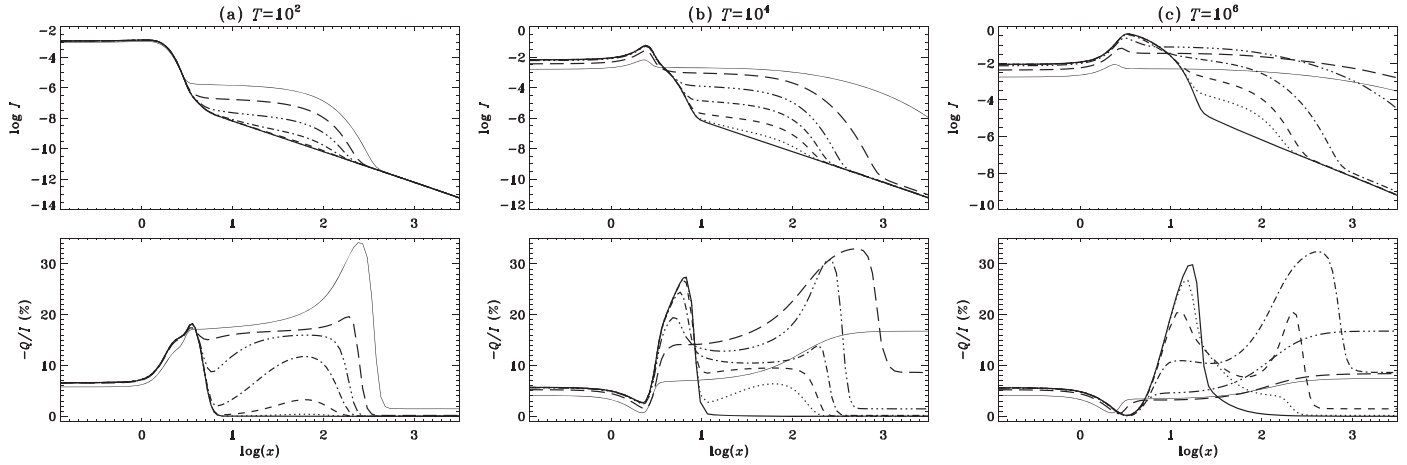

Figure 5. The emergent I and Q/I profiles from a spherically symmetric static medium of outer radius $R = 2$ for different values of β_e. The line of sight is at $\mu = 0.1$. Panels (a), (b), and (c) correspond, respectively, to $T = 10^2$, 10^4, and 10^6. Other model parameters are $\beta_c = 0$, $\epsilon = 10^{-4}$, damping parameter $a = 10^{-3}$, and elastic collision rate $\Gamma_E/\Gamma_R = 0$. Different line types are: solid ($\beta_e = 0$), dotted ($\beta_e = 10^{-8}$), dashed ($\beta_e = 10^{-7}$), dotted–dashed ($\beta_e = 10^{-6}$), dashed–triple–dotted ($\beta_e = 10^{-5}$), long–dashed ($\beta_e = 10^{-4}$), and thin solid ($\beta_e = 10^{-3}$).

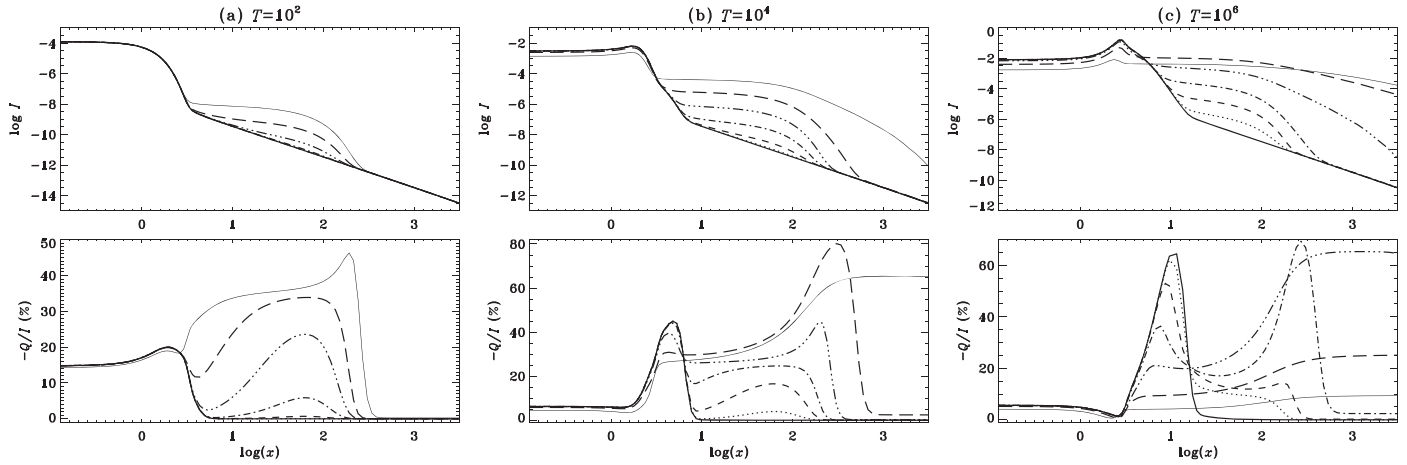

Figure 6. Same as Figure 5, but for $R = 20$.

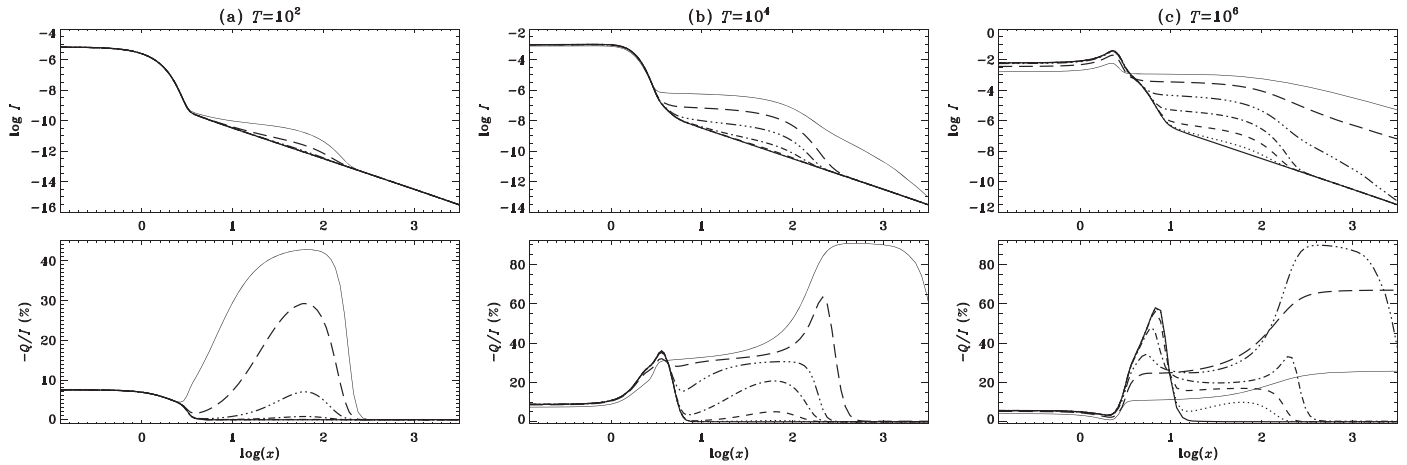

Figure 7. Same as Figure 5, but for $R = 200$.

also increases (see Megha et al. 2019). However, for optically thin ($T = 100$) and moderately thick ($T = 10^4$) cases this increase is seen only up to $R = 20$. For $R = 200$, their magnitude decreases, which may be due to the fact that for these values of T and R the spherical medium becomes considerably dilute. Also, this behavior is seen even for $T = 10^6$ in the presence of elastic collisions (compare dotted–dashed lines in panel (c) of Figures 2–4). Furthermore, for $T = 10^6$ and $R \leqslant 20$, Thomson electron scattering redistribution gives rise to a large constant linear polarization in the wings instead of the secondary peak. In the absence of elastic collisions Thomson electron scattering redistribution leads to a

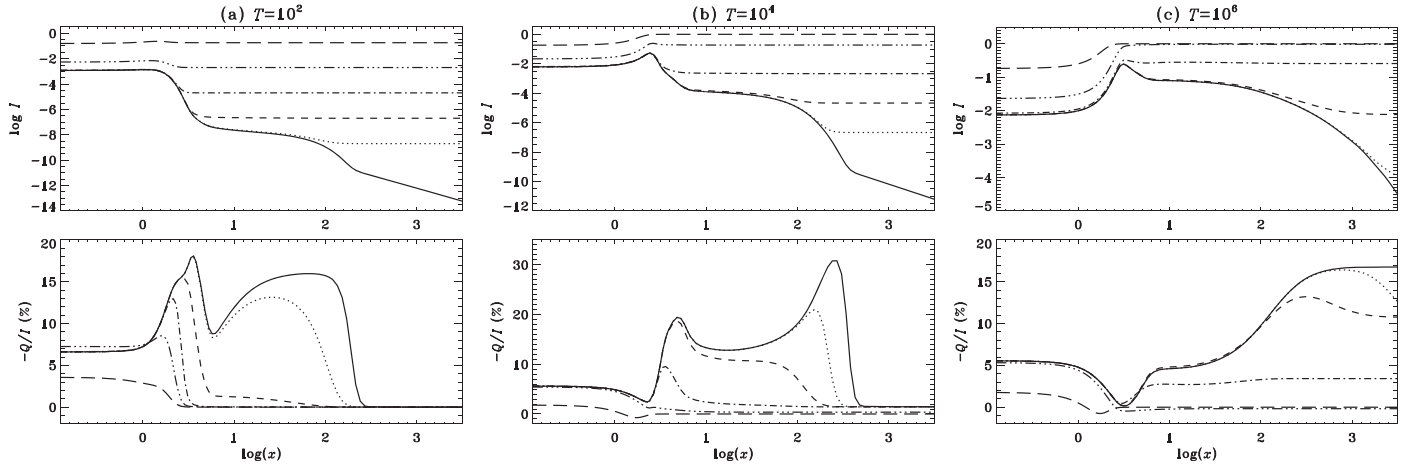

Figure 8. The emergent I and Q/I profiles from a spherically symmetric static medium of outer radius $R = 2$ for different values of β_c. The line of sight is at $\mu = 0.1$. Panels (a), (b), and (c) correspond, respectively, to $T = 10^2$, 10^4, and 10^6. Other model parameters are $\beta_e = 10^{-5}$, $\epsilon = 10^{-4}$, damping parameter $a = 10^{-3}$, and elastic collision rate $\Gamma_E/\Gamma_R = 0$. Different line types are: solid ($\beta_c = 0$), dotted ($\beta_c = 10^{-10}$), dashed ($\beta_c = 10^{-8}$), dotted–dashed ($\beta_c = 10^{-6}$), dashed–triple–dotted ($\beta_c = 10^{-4}$), and long–dashed ($\beta_c = 10^{-2}$).

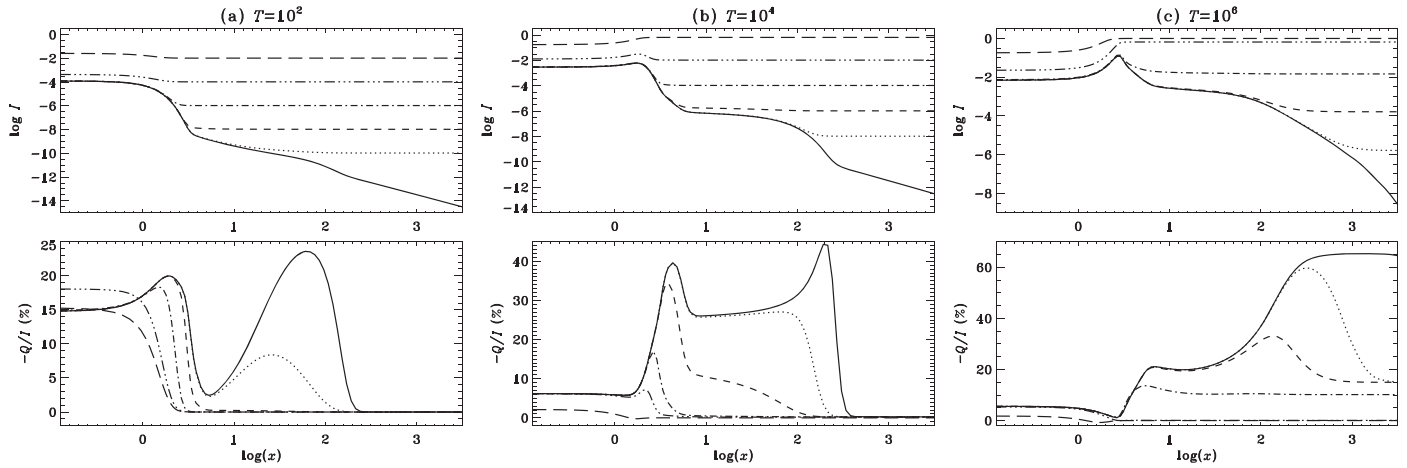

Figure 9. Same as Figure 8, but for $R = 20$.

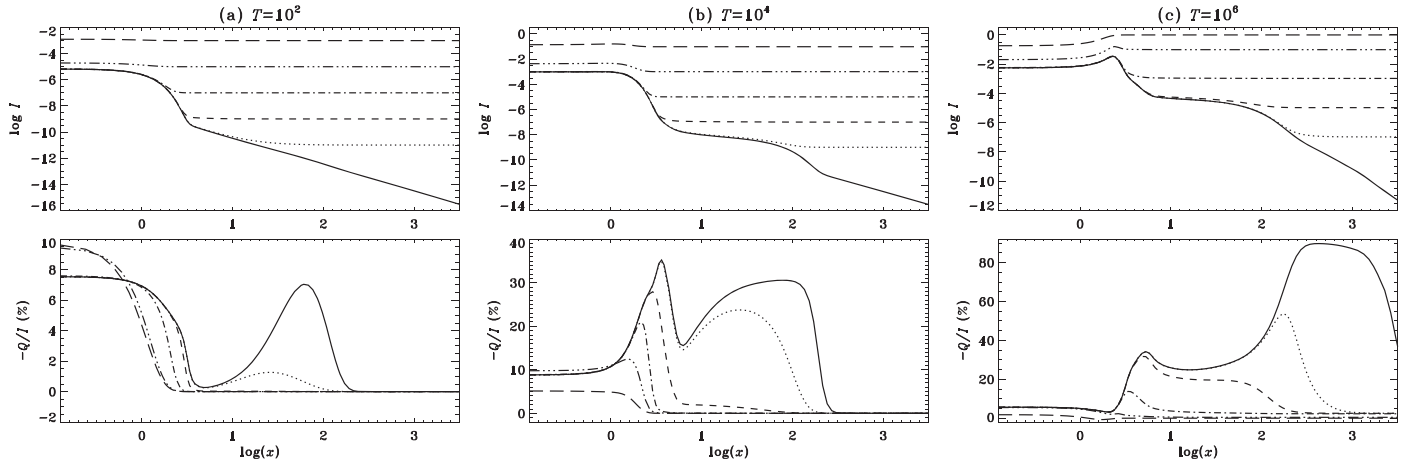

Figure 10. Same as Figure 8, but for $R = 200$.

depolarization in the near wing PRD peak for $T \geqslant 10^4$ (compare solid and dotted lines in panels (b) and (c) of Figures 2–4). Such a behavior has also been noted in the planar case (see Supriya et al. 2012). This may be attributed to the fact that the frequency coherent peaks of the type-II redistribution are narrow and sharp, but those of electron scattering redistribution are relatively much broader (compare upper and lower panels of Figure 1). This then redistributes the line wing photons resulting in a depolarization of the near wing PRD peak. For a given R, the extent of depolarization increases

Table 1
The Maximum Value and Corresponding Frequency Position of the Wing Bulge in Intensity and the Secondary Peak in Q/I for $R = 2$ and Different T and β_e Considered in Figure 5

β_e	$T = 100$				$T = 10^4$				$T = 10^6$			
	Wing Bulge in I		Secondary Peak in Q/I		Wing Bulge in I		Secondary Peak in Q/I		Wing Bulge in I		Secondary Peak in Q/I	
	Max. Value	Position ($x_{\rm max,bulge}$)	Peak Value (%)	Position ($x_{\rm sp}$)	Max. Value	Position ($x_{\rm max,bulge}$)	Peak Value (%)	Position ($x_{\rm sp}$)	Max. Value	Position ($x_{\rm max,bulge}$)	Peak Value (%)	Position ($x_{\rm sp}$)
10^{-8}	0.177E − 9	60.82	−0.396E + 0	60.82	0.482E − 7	60.82	−0.638E + 1	60.82	0.419E − 4	60.82	−0.395E + 1	152.9
	(0.172E − 9)		(−0.134E−3)		(0.173E − 7)		(−0.134E−1)		(0.181E − 5)		(−0.208E + 0)	
10^{-7}	0.215E − 9	60.82	−0.326E + 1	60.82	0.327E − 6	60.82	−0.949E + 1	60.82	0.438E − 3	60.82	−0.206E + 2	215.3
	(0.172E − 9)		(−0.134E−3)		(0.173E − 7)		(−0.134E−1)		(0.181E − 5)		(−0.105E + 0)	
10^{-6}	0.597E − 9	60.82	−0.117E + 2	60.82	0.316E − 5	60.82	−0.139E + 2	192.3	0.307E − 2	96.22	−0.324E + 2	429.1
	(0.172E − 9)		(−0.134E−3)		(0.173E − 7)		(−0.132E−2)		(0.704E − 6)		(−0.265E−1)	
10^{-5}	0.442E − 8	60.82	−0.159E + 2	68.33	0.289E − 4	68.33	−0.308E + 2	271.0	0.272E − 2	678.5	−0.167E + 2[a]	3751.4
	(0.172E − 9)		(−0.106E−3)		(0.137E − 7)		(−0.669E−3)		(0.136E − 7)		(−0.316E−3)	
10^{-4}	0.428E − 7	60.82	−0.196E + 2	192.3	0.223E − 3	96.22	−0.329E + 2	480.7	0.148E − 2	3751.4	−0.840E + 1[a]	3751.4
	(0.172E − 9)		(−0.133E−4)		(0.690E − 8)		(−0.211E−3)		(0.409E − 9)		(−0.316E−3)	
10^{-3}	0.356E − 6	68.33	−0.341E + 2	241.2	0.945E − 4	678.5	−0.167E + 2[a]	3751.4	0.276E − 3	3751.4	−0.747E + 1[a]	3751.4
	(0.137E − 9)		(−0.845E−5)		(0.136E − 9)		(−0.316E−5)		(0.409E − 9)		(−0.316E−3)	

Note. For reference we give in parentheses the I and Q/I values corresponding to $\beta_e = 0$ at $x_{\rm max,bulge}$ and $x_{\rm sp}$, respectively.
[a] Q/I for these cases exhibits a constant profile in the far wing instead of a secondary peak (see panels (b) and (c) of Figure 5).

Table 2
Same as Table 1, but for $R = 20$ (see Figure 6)

β_e	$T = 100$				$T = 10^4$				$T = 10^6$			
	Wing Bulge in I		Secondary Peak in Q/I		Wing Bulge in I		Secondary Peak in Q/I		Wing Bulge in I		Secondary Peak in Q/I	
	Max. Value	Position ($x_{\rm max,bulge}$)	Peak Value (%)	Position ($x_{\rm sp}$)	Max. Value	Position ($x_{\rm max,bulge}$)	Peak Value (%)	Position ($x_{\rm sp}$)	Max. Value	Position ($x_{\rm max,bulge}$)	Peak Value (%)	Position ($x_{\rm sp}$)
10^{-8}	0.912E − 11	60.82	−0.705E − 1	60.82	0.107E − 8	60.82	−0.394E + 1	60.82	0.618E − 6	60.82	−0.754E + 1	121.2
	(0.910E − 11)		(−0.214E − 4)		(0.910E − 9)		(−0.214E − 2)		(0.914E − 7)		(−0.536E − 1)	
10^{-7}	0.928E − 11	60.82	−0.692E + 0	60.82	0.257E − 8	60.82	−0.165E + 2	60.82	0.545E − 5	60.82	−0.144E + 2	171.1
	(0.910E − 11)		(−0.214E − 4)		(0.910E − 9)		(−0.214E − 2)		(0.914E − 7)		(−0.268E − 1)	
10^{-6}	0.109E − 10	60.82	−0.588E + 1	60.82	0.175E − 7	60.82	−0.246E + 2	68.33	0.501E − 4	68.33	−0.692E + 2	271.0
	(0.910E − 11)		(−0.214E − 4)		(0.910E − 9)		(−0.169E − 2)		(0.723E − 7)		(−0.106E − 1)	
10^{-5}	0.272E − 10	60.82	−0.235E + 2	60.82	0.137E − 6	68.33	−0.443E + 2	192.3	0.425E − 3	107.7	−0.653E + 2[a]	1335.5
	(0.910E − 11)		(−0.214E − 4)		(0.721E − 9)		(−0.212E − 3)		(0.290E − 7)		(−0.427E − 3)	
10^{-4}	0.191E − 9	60.82	−0.338E + 2	68.33	0.128E − 5	76.60	−0.801E + 2	304.5	0.364E − 4	3751.4	−0.251E + 2[a]	3751.4
	(0.910E − 11)		(−0.169E − 4)		(0.573E − 9)		(−0.845E − 4)		(0.215E − 10)		(−0.505E − 4)	
10^{-3}	0.184E − 8	60.82	−0.462E + 2	192.3	0.751E − 5	121.2	−0.653E + 2[a]	1524.3	0.155E − 3	3751.4	−0.937E + 1[a]	3751.4
	(0.910E − 11)		(−0.212E − 5)		(0.228E − 9)		(−0.326E − 5)		(0.215E − 10)		(−0.505E − 4)	

Note. For reference we give in parentheses the I and Q/I values corresponding to $\beta_e = 0$ at $x_{\rm max,bulge}$ and $x_{\rm sp}$, respectively.
[a] Q/I for these cases exhibits a constant profile in the far wing instead of a secondary peak (see panels (b) and (c) of Figure 6).

Table 3
Same as Table 1, but for $R = 200$ (see Figure 7)

β_e	$T = 100$				$T = 10^4$				$T = 10^6$			
	Wing Bulge in I		Secondary Peak in Q/I		Wing Bulge in I		Secondary Peak in Q/I		Wing Bulge in I		Secondary Peak in Q/I	
	Max. Value	Position ($x_{\rm max,bulge}$)	Peak Value (%)	Position ($x_{\rm sp}$)	Max. Value	Position ($x_{\rm max,bulge}$)	Peak value (%)	Position ($x_{\rm sp}$)	Max. Value	Position ($x_{\rm max,bulge}$)	Peak Value (%)	Position ($x_{\rm sp}$)
10^{-8}	0.869E − 12	60.82	−0.834E − 2	60.82	0.886E − 10	60.82	−0.598E + 0	60.82	0.192E − 7	60.82	−0.993E + 1	60.82
	(0.869E − 12)		(−0.219E − 5)		(0.869E − 10)		(−0.219E − 3)		(0.869E − 8)		(−0.219E − 1)	
10^{-7}	0.870E − 12	60.82	−0.833E − 1	60.82	0.103E − 9	60.82	−0.510E + 1	60.82	0.114E − 6	60.82	−0.169E + 2	60.82
	(0.869E − 12)		(−0.219E − 5)		(0.869E − 10)		(−0.219E − 3)		(0.869E − 8)		(−0.219E − 1)	
10^{-6}	0.885E − 12	60.82	−0.819E + 0	60.82	0.256E − 9	60.82	−0.207E + 2	60.82	0.109E − 5	60.82	−0.331E + 2	192.3
	(0.869E − 12)		(−0.219E − 5)		(0.869E − 10)		(−0.219E − 3)		(0.869E − 8)		(−0.217E − 2)	
10^{-5}	0.103E − 11	60.82	−0.704E + 1	60.82	0.178E − 8	60.82	−0.305E + 2	76.60	0.868E − 5	76.60	−0.897E + 2	429.1
	(0.869E − 12)		(−0.219E − 5)		(0.869E − 10)		(−0.138E − 3)		(0.547E − 8)		(−0.434E − 3)	
10^{-4}	0.248E − 11	60.82	−0.292E + 2	60.82	0.139E − 7	68.33	−0.634E + 2	215.3	0.613E − 4	121.2	−0.669E + 2[a]	3751.4
	(0.869E − 12)		(−0.219E − 5)		(0.688E − 10)		(−0.173E − 4)		(0.218E − 8)		(−0.516E − 5)	
10^{-3}	0.170E − 10	60.82	−0.428E + 2	68.33	0.123E − 6	76.60	−0.907E + 2	480.7	0.443E − 5	3751.4	−0.257E + 2[a]	3751.4
	(0.869E − 12)		(−0.173E − 5)		(0.547E − 10)		(−0.345E − 5)		(0.205E − 11)		(−0.516E − 5)	

Note. For reference we give in parentheses the I and Q/I values corresponding to $\beta_e = 0$ at $x_{\rm max,bulge}$ and $x_{\rm sp}$, respectively.
[a] Q/I for these cases exhibits a constant profile in the far wing instead of a secondary peak (see panel (c) of Figure 7).

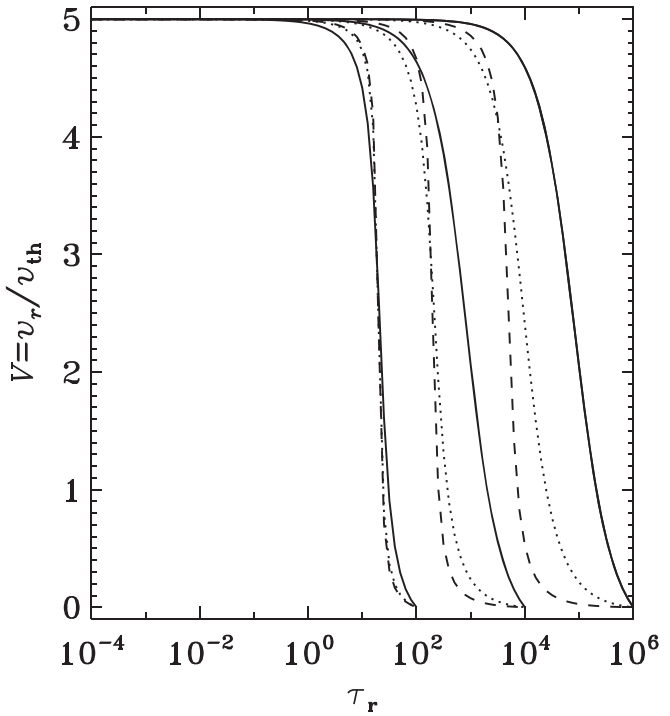

Figure 11. The arctan velocity law (see Equation (20)) as a function of radial optical depth τ_r for $T = 100$, 10^4, and 10^6. For each T, the solid, dotted, and dashed lines correspond to $R = 2$, 20, and 200 respectively. The maximum expansion velocity is five mean thermal units. Other parameters are given in Section 3.3.

with optical thickness T. However, for $T = 10^4$ and $R = 200$, the Q/I near wing PRD peak is only marginally affected by Thomson electron scattering redistribution (compare solid and dotted lines in panel (b) of Figure 4), because of the highly diluted emission lobes in this particular case.

To further study the influence of Thomson electron scattering redistribution on linear polarization profiles, we present in Figures 5–7 the dependence of I and Q/I profiles on β_e again for $R = 2$, 20, 200, respectively, and in each case for $T = 100$, 10^4, 10^6 (panels (a)–(c), respectively). We have varied β_e in the range 10^{-8} to 10^{-3}. The case of $\beta_e = 0$ (i.e., neglecting Thomson electron scattering redistribution) is shown for comparison as a thick solid line. As β_e increases the influence of Thomson electron scattering redistribution on the wings of I and Q/I profiles increases. The bulge in the intensity profile increases and the effect of Thomson electron scattering redistribution is seen over larger and larger frequency bandwidths. For the optically thick case $T = 10^6$, when $\beta_e \geqslant 10^{-4}$, Thomson electron scattering redistribution is seen to affect the entire intensity profile (see long–dashed and thin solid lines in panel (c) of Figures 5–7). Again for a given radial optical thickness T, as R increases the effects of Thomson electron scattering redistribution on the wings of intensity profiles relatively decreases. To clearly bring out the above-mentioned effects of Thomson electron scattering redistribution, we present in Tables 1–3 the maximum value and the corresponding frequency position ($x_{\rm max,bulge}$) of the wing bulge in intensity I for all the different cases illustrated in Figures 5–7, respectively. The maximum value of the wing bulge is determined using the $\beta_e = 0$ case as the reference. These tables also give the peak value and the corresponding frequency position ($x_{\rm sp}$) of the secondary peak in Q/I, the dependence of which on β_e is discussed in the following paragraph.

The Stokes Q/I profiles exhibit a strong dependence on β_e for the different T and R considered here. For $R = 2$ and $T = 100$, the secondary peak in Q/I is formed for β_e as small as 10^{-8} (see Table 1). However, it is not visible in the scale adopted for panel (a) of Figure 5. The secondary peak becomes graphically visible for $\beta_e = 10^{-7}$ (see the dashed line in panel (a) of Figure 5). This peak then increases in magnitude with β_e and also becomes broader, subsequently exhibiting a flat topped appearance for $\beta_e = 10^{-5}$ (see the dashed–triple–dotted line in panel (a) of Figure 5). For still larger values of β_e we obtain a sharper secondary peak at shifted frequencies, which further increases in magnitude and width (see the thin solid line in panel (a) of Figure 5). The above-noted behavior of the secondary peak in Q/I can also be readily appreciated from Table 1. For $T = 100$, as R increases, the secondary peak starts to become graphically visible for still larger values of β_e; namely for $R = 20$ and 200 it becomes visible when $\beta_e = 10^{-6}$ and 10^{-5}, respectively. In other words as R increases, higher values of β_e are needed to produce effects similar to those obtained for smaller R (compare Tables 1, 2, and 3). For $T = 100$ and $\beta_e < 10^{-5}$ the secondary peak in Q/I decreases in magnitude as R increases from 2 to 200, while for $\beta_e \geqslant 10^{-5}$ this peak increases in magnitude until $R = 20$ and then decreases for $R = 200$ (compare the fourth column in Tables 1–3). Furthermore, the frequency position $x_{\rm sp}$ of the secondary peak in Q/I decreases with increasing R until $x_{\rm sp} = 60.82$ (compare fifth column in Tables 1–3).

For $T \geqslant 10^4$, the depolarization of the near wing PRD peak increases with β_e (see panels (b) and (c) of Figures 5–7). The secondary peak on the other hand shows a nonmonotonic variation with increase in β_e. For $T = 10^4$, $R = 2$, and $\beta_e \leqslant 10^{-4}$, this peak increases in magnitude, becomes broader, followed by a flat topped appearance, and then becomes a shifted sharper peak whose width and magnitude again increases until $\beta_e = 10^{-4}$ (see Table 1). Such a variation in the shape and magnitude of the secondary peak with increasing values of β_e is similar to the corresponding $T = 100$ case. However, when $\beta_e = 10^{-3}$, Thomson electron scattering redistribution produces a constant linear polarization profile in the far wings instead of a peak (see thin solid line in Q/I of panel (b) in Figure 5). Like in the $T = 100$ case, for larger values of R the similar effects of Thomson electron scattering redistribution are seen only for higher values of β_e (compare Tables 1, 2, and 3). Consequently, for $R = 200$ and $T = 10^4$, the shape of the Q/I in the far wings for $\beta_e = 10^{-3}$ is a broad secondary peak at a highly shifted frequency and not a constant far wing polarization as obtained for $R < 200$ (compare thin solid lines in panel (b) of Figures 5–7).

The dependence of Q/I profiles on β_e for the optically thick case of $T = 10^6$ and the different R is somewhat similar to that of the $T = 10^4$ case. However, for a given R as T increases, the similar effects of Thomson electron scattering redistribution become apparent already for smaller values of β_e (compare the fourth, eighth, and twelfth columns in Tables 1–3). This is because as T increases for a given R, the mean number of scatterings also increases (Kunasz & Hummer 1974). Consequently, for larger T the influence of Thomson electron scattering redistribution becomes more pronounced even for smaller β_e. For example a constant far wing polarization is seen

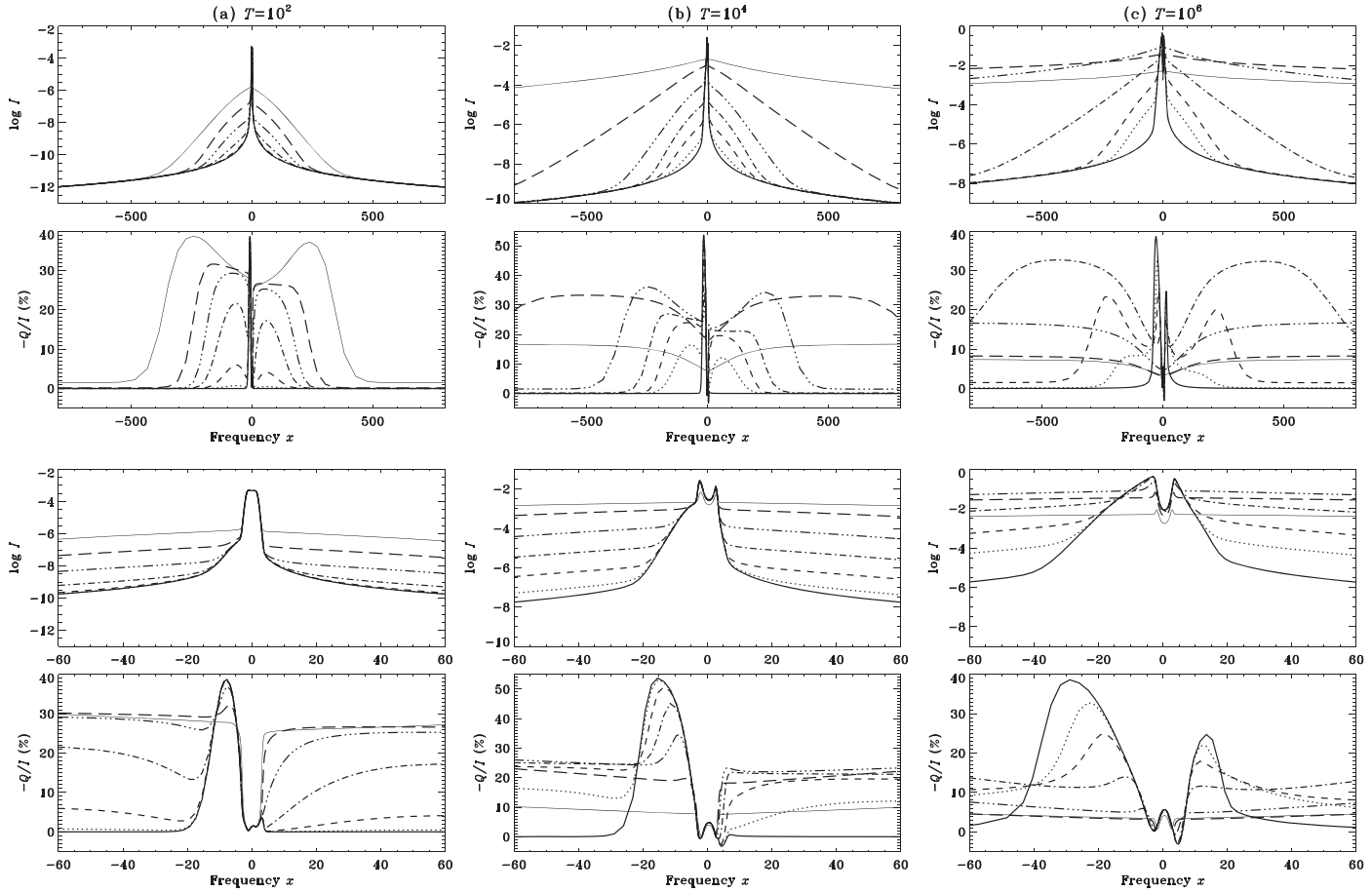

Figure 12. The emergent I and Q/I profiles from a spherically symmetric moving medium of outer radius $R = 2$ for different values of β_e. The line of sight is at $\mu = 0.1$. Panels (a), (b), and (c) correspond, respectively, to $T = 10^2$, 10^4, and 10^6. Bottom two rows are identical to the corresponding top two rows, except that we consider a relatively shorter frequency bandwidth to display the line core and near wing regions in greater details. An arctan velocity law with maximum expansion velocity of five mean thermal units is used (see Figure 11). Other model parameters are $\beta_c = 0$, $\epsilon = 10^{-4}$, damping parameter $a = 10^{-3}$, and elastic collision rate $\Gamma_E/\Gamma_R = 0$. Different line types are: solid ($\beta_e = 0$), dotted ($\beta_e = 10^{-8}$), dashed ($\beta_e = 10^{-7}$), dotted–dashed ($\beta_e = 10^{-6}$), dashed–triple–dotted ($\beta_e = 10^{-5}$), long–dashed ($\beta_e = 10^{-4}$), and thin solid ($\beta_e = 10^{-3}$).

already for $\beta_e = 10^{-5}$ in the case of $T = 10^6$ and $R \leqslant 20$ instead of at $\beta_e = 10^{-3}$ for the corresponding $T = 10^4$ case.

In the planar case, Supriya et al. (2012) noted that for $T \geqslant 10^4$ the secondary peak in Q/I produced due to Thomson electron scattering redistribution is related to the electron scattering optical depth $T_e = \beta_e T$ and that it occurs when the condition $0.1 \lesssim T_e \lesssim 1$ is satisfied. However, the above condition is valid for a nonzero background continuum of $\beta_c = 10^{-8}$ (that was considered in Supriya et al. 2012). Furthermore, we find that the above-said condition is valid for continuum optical depths $\beta_c T \leqslant 10^{-3}$. In the absence of background continuum, we find that the lower limit of the above-said condition gets extended to 0.01. However, in the spherical case no such condition may be prescribed for the occurrence of the secondary peak. Indeed, a secondary peak is obtained for β_e as small as 10^{-8} for the case of $T = 10^4$ (see the dotted line in Q/I of panel (b) in Figures 5 and 6). This clearly demonstrates the considerably more complex nature of spherical transfer when compared to the transfer in a planar medium.

In the atmospheres of early-type stars the bound–free and free–free transitions in H I, He I, and He II are the main sources of background continuum opacity (see p. 170 of Hubeny & Mihalas 2015). Thus in Figures 8–10 we show the influence of a nonzero background continuum on linear polarization profiles that are affected by the Thomson electron scattering redistribution (with $\beta_e = 10^{-5}$). We have varied the background continuum parameter β_c in the range 10^{-10} to 10^{-2}. The case of the pure line affected by Thomson electron scattering redistribution (namely, $\beta_c = 0$ and $\beta_e = 10^{-5}$) is shown as the solid line for reference. The effect of a nonzero background continuum on both intensity and Q/I profiles can be clearly seen for β_c as small as 10^{-10} (compare solid and dotted lines in Figures 8–10). In particular the bulge in the intensity profile that is caused by Thomson electron scattering redistribution decreases as the intensity in the far wings is raised due to continuum absorption. This bulge completely disappears with further increase in β_c. The value of β_c for which this occurs however depends on the optical thickness T and outer radius R. For example for $R = 2$, we see that the bulge disappears for $\beta_c = 10^{-8}$ and 10^{-6} in the cases of $T = 100$ and $T \geqslant 10^4$, respectively. With further increase in β_c, the influence of continuum absorption is progressively seen at smaller frequencies, such that for $\beta_c = 10^{-2}$ we obtain a weak emission or absorption line depending on T and R. As for the Q/I profiles, the background continuum dilutes the polarized radiation field by contributing unpolarized continuum photons. Therefore, with an increase in β_c the secondary peak due to Thomson electron scattering redistribution as well as the near wing PRD peak reduces in magnitude, subsequently leading to a

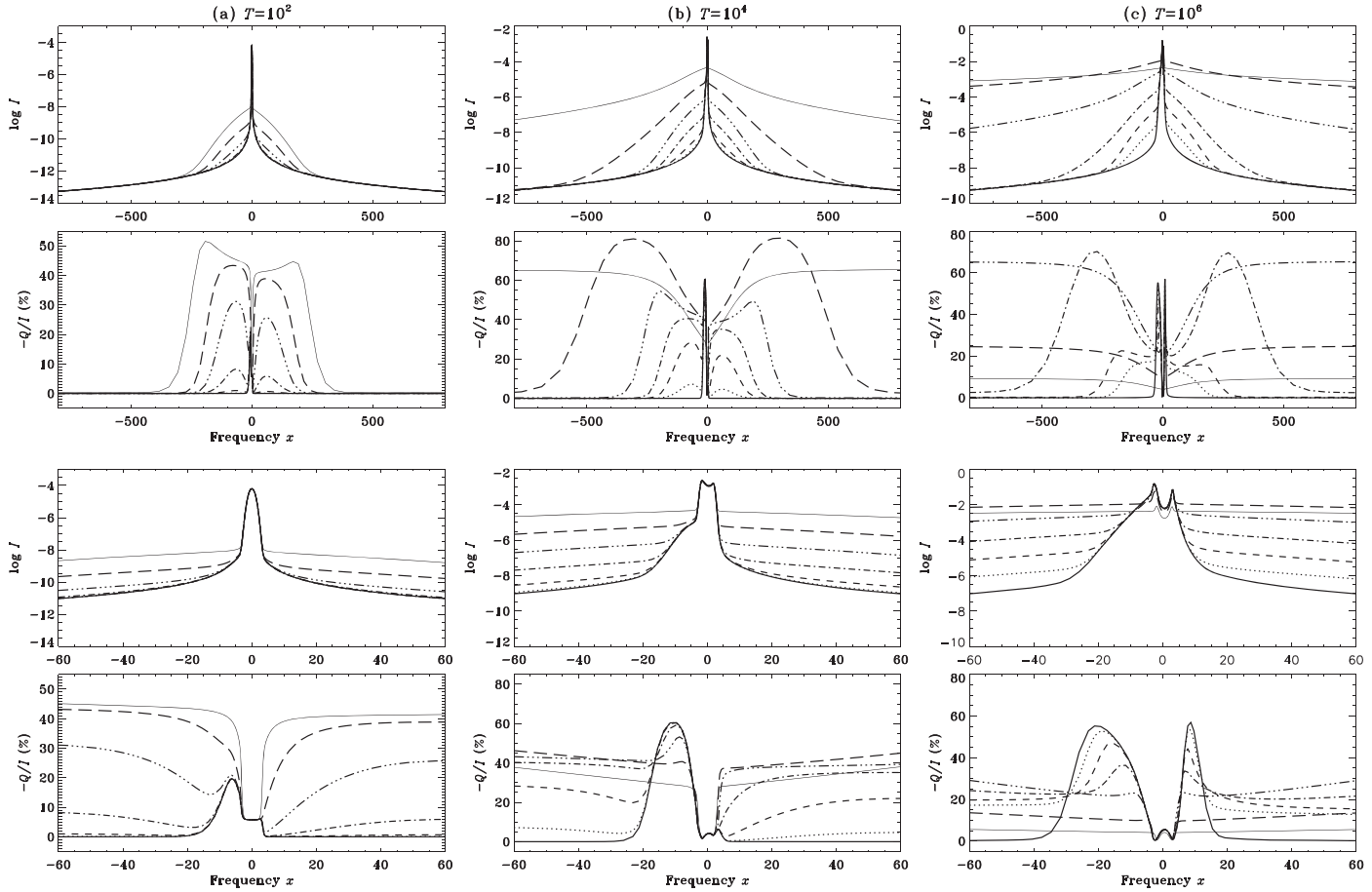

Figure 13. Same as Figure 12, but for $R = 20$.

polarization profile confined to the line core (see for example long–dashed line in Figures 8–10). Again the value of β_c at which the secondary peak becomes completely nonexistent depends on T and R. In the case of $T = 10^6$ and $R \leqslant 20$, the constant linear polarization profile in the far wing produced by the Thomson electron scattering redistribution becomes a secondary peak for $\beta_c = 10^{-10}$ and 10^{-8} (see dotted and dashed lines in panel (c) of Figures 8 and 9), which then rapidly vanishes with further increase in β_c.

3.3. Expanding Atmosphere

In this section we illustrate the influence of Thomson electron scattering redistribution on polarized line profiles formed in spherically symmetric expanding atmospheres. In such atmospheres, the intensity and linearly polarized profiles are known to be asymmetric about the line center due to the velocity field effects. Therefore, here we present the Stokes profiles for both positive and negative values of x as well as for both larger (to illustrate the effects of Thomson electron scattering redistribution) and smaller (to show the details in and around the line core and near wing regions) frequency bandwidths. We consider an arctan velocity law of the form (Mihalas et al. 1976)

$$V(r) = V_{\max}\,[\tan^{-1}(ar + b) - \tan^{-1}(a + b)], \qquad (20)$$

where $V_{\max}$ is the maximum expansion velocity. The arctan velocity law given in the above equation is an analytic representation of the velocity field introduced by Castor et al. (1975) to describe radiation-driven winds in atmospheres of O stars. The radius and radial line optical depth at which the velocity gradient is at maximum is denoted by r_v and τ_v, respectively. The parameters a and b take values according to the choice made for r_v $(= -b/a)$ or τ_v and a number c $(= a + b)$. Following Mihalas et al. (1976) we have chosen $c = 6$ and $\tau_v = 20$, 200, and 5×10^3 for $T = 100$, 10^4, and 10^6, respectively. For this choice of parameters and for a maximum expansion velocity of five mean thermal units, the graphical form of the arctan velocity law for different T and R considered in the present paper is displayed in Figure 11.

Figures 12–14 show the effects of Thomson electron scattering redistribution on I and Q/I profiles emerging from a spherically symmetric expanding atmosphere for $R = 2$, 20, 200, respectively, and in each case for $T = 100$, 10^4, 10^6 (panels (a)–(c), respectively). When compared to the corresponding static case (see Figures 5–7), the asymmetry about the line center caused by the radial velocity field is apparent in both I and Q/I profiles. In particular the Q/I profiles are highly sensitive to the velocity fields and exhibit a large asymmetry in the blue and red side near wing PRD peaks (see thick solid lines in bottom Q/I panels of Figures 12–14). The radial velocity field in a spherically symmetric medium produces Doppler redshift in the far side of the hemisphere (as it recedes from the observer) and Doppler blueshift in the near side (as it approaches the observer). Furthermore, the far side is known to contribute to the red region of the profile, while the near side to the blue region. In addition, the Doppler shift $\mu(r, p)V(r)$

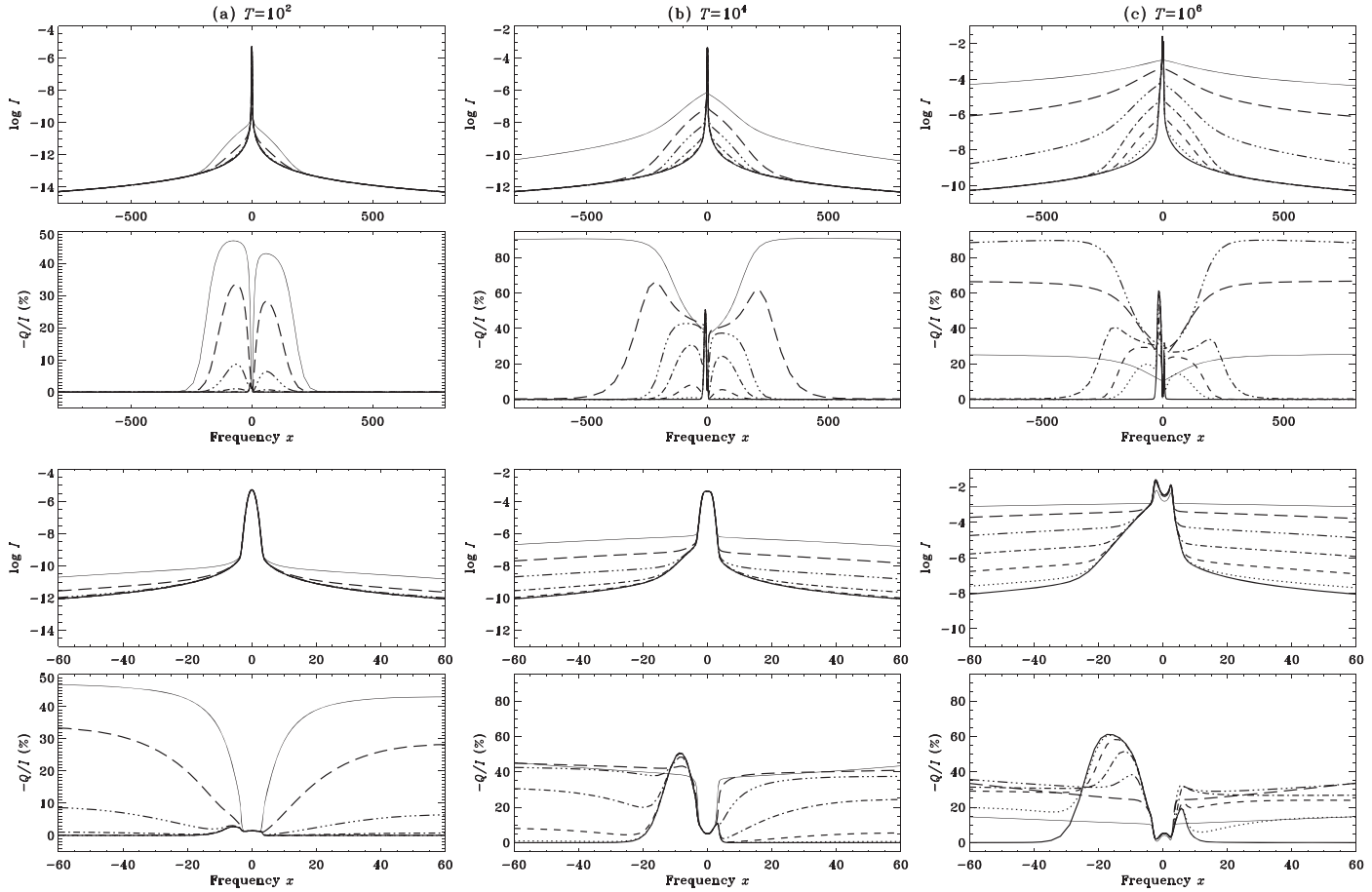

Figure 14. Same as Figure 12, but for $R = 200$.

reduces with decreasing values of μ. Since in a spherical atmosphere μ changes along a given impact parameter ray, the velocity gradient in the z-direction is further enhanced over and above the radial velocity gradient implicit in the considered velocity field. All these effects together modify the anisotropy of the radiation field resulting in large asymmetry in the Q/I profiles.

The effects of Thomson electron scattering redistribution on intensity profiles affected by velocity fields are somewhat similar to the corresponding static case. When Thomson electron scattering redistribution is neglected the asymmetry about the line center produced by the velocity field is mostly confined to $|x| \lesssim 20$, 30, 50 for $T = 100$, 10^4, 10^6, respectively. When Thomson electron scattering redistribution is included this asymmetry between the red and the blue side is reduced as the electron scattering lifts the intensity in the wings. However, a slight asymmetry persists for $|x|$ as large as ≈ 60 for certain values of β_e, R, and T (see, e.g., dashed–triple–dotted line in bottom I of panel (a) in Figure 12).

In the case of Q/I profiles formed in expanding spherical medium, Thomson electron scattering redistribution again exhibits a behavior similar to the static case, namely it gives rise to secondary peak whose dependence on β_e for different R and T follows the corresponding static case. However, in the expanding medium the secondary peaks are asymmetric about the line center. For $T = 100$ this asymmetry is seen for all the different R and β_e considered here, while for $T = 10^4$ and 10^6 the asymmetry nearly vanishes for $\beta_e = 10^{-3}$ and 10^{-5}, respectively. Furthermore, the large asymmetry between the red and blue side near wing PRD peaks in Q/I profiles decreases with increasing values of β_e (see bottom Q/I panels of Figures 12–14).

4. Conclusions

In the present paper we have made a detailed investigation on the influence of Thomson electron scattering redistribution on resonance line polarization profiles formed in spherically symmetric static and expanding media. The concerned polarized transfer equation derived using the tangent-ray method is then solved by applying the Jacobi based CMF polarized accelerated lambda iteration technique. To isolate the effects of Thomson electron scattering, in the present paper, we have assumed the other continuum contributions (such as Rayleigh scattering on neutral hydrogen and helium) to be unpolarized. We plan to relax this assumption in a future extension of the present work.

Thomson electron scattering redistribution is shown to significantly affect both the intensity and fractional linear polarization profiles. In particular, the intensity in the wings is raised in the presence of electron scattering, while a noticeable secondary peak is produced in the Q/I profiles. For a given radial line-integrated optical thickness T, as the outer radius R of the spherical medium increases, higher values of electron scattering opacity β_e are needed to produce effects similar to those obtained for smaller R. This is because the spherical medium becomes more and more dilute so that the mean number of scatterings decreases (Kunasz & Hummer 1974). On

the other hand for a given R, as T increases the mean number of scatterings increases; consequently similar effects of Thomson electron scattering redistribution are seen for progressively smaller values of β_e. These effects of Thomson electron scattering redistribution are common to both the static and expanding spherical medium. In the presence of velocity fields, the secondary peak produced by Thomson electron scattering redistribution in Q/I is asymmetric about the line center. Moreover, Thomson electron scattering redistribution reduces the large asymmetry produced by the velocity fields between the red and blue side near wing PRD peaks in Q/I and also between the red and blue regions of the intensity profile. These numerical results clearly demonstrate the importance of including Thomson electron scattering redistribution in spectral line polarization problems relevant for stellar atmospheres.

We acknowledge the use of the high-performance computing facility at the Indian Institute of Astrophysics. M.S. acknowledges the support from the Science and Engineering Research Board (SERB), Department of Science and Technology, Government of India via a SERB-Women Excellence Award research grant WEA/2020/000012. The authors are grateful to the reviewers for constructive and useful comments.

ORCID iDs

M. Sampoorna https://orcid.org/0000-0001-8755-0926
A. Megha https://orcid.org/0000-0002-8457-9771
H. D. Supriya https://orcid.org/0000-0003-2752-7681

References

Auer, L. H., & Mihalas, D. 1968, ApJ, 153, 245
Bommier, V. 1997, A&A, 328, 706
Castor, J. I., Abbott, D. C., & Klein, R. I. 1975, ApJ, 195, 157
Chandrasekhar, S. 1950, Radiative Transfer (Oxford: Clarendon Press)
Domke, H., & Hubeny, I. 1988, ApJ, 334, 527
Fluri, D. M., & Stenflo, J. O. 1999, A&A, 341, 902
Frisch, H. 2007, A&A, 476, 665
Hauschildt, P. H., & Baron, E. 2004, A&A, 417, 317
Hillier, D. J. 1991, A&A, 247, 455
Hillier, D. J. 1996, A&A, 308, 521
Hubeny, I., & Mihalas, D. 2015, Theory of Stellar Atmospheres: An Introduction to Astrophysical Non-equilibrium Quantitative Spectroscopic Analysis (Princeton, NJ: Princeton Univ. Press)
Hummer, D. G. 1962, MNRAS, 125, 21
Hummer, D. G., & Mihalas, D. 1967, ApJL, 150, L57
Hummer, D. G., & Rybicki, G. B. 1971, MNRAS, 152, 1
Kostogryz, N. M., & Berdyugina, S. V. 2015, A&A, 575, A89
Kostogryz, N. M., Milic, I., Berdyugina, S. V., & Hauschildt, P. H. 2016, A&A, 586, A87
Kunasz, P. B., & Hummer, D. G. 1974, MNRAS, 166, 19
Megha, A., Sampoorna, M., Nagendra, K. N., Anusha, L. S., & Sankarasubramanian, K. 2019, ApJ, 879, 48
Mihalas, D. 1978, Stellar Atmospheres (San Francisco, CA: W.H. Freeman)
Mihalas, D., Kunasz, P. B., & Hummer, D. G. 1975, ApJ, 202, 465
Mihalas, D., Kunasz, P. B., & Hummer, D. G. 1976, ApJ, 210, 419
Nagendra, K. N., Rangarajan, K. E., & Rao, D. M. 1993, MNRAS, 262, 855
Paletou, F., & Auer, L. H. 1995, A&A, 297, 771
Sampoorna, M., Nagendra, K. N., & Frisch, H. 2008, JQSRT, 109, 2349
Stenflo, J. O. 1994, Solar Magnetic Fields: Polarized Radiation Diagnostics (Dordrecht: Kluwer)
Stenflo, J. O. 2005, A&A, 429, 713
Supriya, H. D., Nagendra, K. N., Sampoorna, M., & Ravindra, B. 2012, MNRAS, 425, 527